

An Adversarial Learning Based Approach for Unknown View Tomographic Reconstruction

Mona Zehni, Zhizhen Zhao

Abstract—The goal of 2D tomographic reconstruction is to recover an image given its projection lines from various views. It is often presumed that projection angles associated with the projection lines are known in advance. Under certain situations, however, these angles are known only approximately or are completely unknown. It becomes more challenging to reconstruct the image from a collection of random projection lines. We propose an adversarial learning based approach to recover the image and the projection angle distribution by matching the empirical distribution of the measurements with the generated data. Fitting the distributions is achieved through solving a min-max game between a generator and a critic based on Wasserstein generative adversarial network structure. To accommodate the update of the projection angle distribution through gradient back propagation, we approximate the loss using the Gumbel-Softmax reparameterization of samples from discrete distributions. Our theoretical analysis verifies the unique recovery of the image and the projection distribution up to a rotation and reflection upon convergence. Our extensive numerical experiments showcase the potential of our method to accurately recover the image and the projection angle distribution under noise contamination.

Index Terms—Tomographic reconstruction, adversarial learning, hartley-bessel expansion, gumbel-softmax, categorical distribution, computed tomography

I. INTRODUCTION

Multitude of imaging modalities rely on reconstructing an unknown signal either in 2D or 3D domain given a set of partial measurements. Examples of such are medical imaging, cryo-electron microscopy (cryo-EM) and optical microscopy. More specifically, in a tomographic reconstruction setup, the measurements i.e. projections, are the line/plane integrals of the underlying object along various angles. In this paper, we focus on 2D X-ray tomography. Recovering the unknown object given a large set of noisy projections is the ultimate goal in tomographic reconstruction.

Tomographic inversion with known viewing angles is typically a linear inverse problem and is solved by filtered back-projection (FBP), direct Fourier methods [1], or solving a regularized optimization problem [2]–[5]. However, the knowledge of the projection angles is not always available or accurate. To avoid adverse effects on the quality of the reconstructed 2D image, it is important to account for uncertainties in the projection angles. To address this, one family of solutions determine the projection angles first [6]–[9] and then reconstruct the image given the estimated projection views. Other approaches include iterative methods that solve for the 2D image and

the projection angles in alternating steps [10]. While proven effective, these methods are computationally expensive and sensitive to initialization due to the inherent non-convexity of the problem. In another class of methods, to circumvent the estimation/refinement of the projection angles, a set of rotation invariant features are estimated from the noisy projections. These features are later on used to reconstruct the unknown image [11]–[14]. Note that these methods require only one pass through the projection dataset and are therefore computationally more efficient. However, they are still sensitive to initialization and prone to getting stuck at local optima.

There is a recent surge in application of deep learning (DL) for the tomographic reconstruction task [15]. Majority of DL-based solutions assume the projection angles are known. These methods depending on the input to the DL model and the infusion of the physics of the problem can be broadly classified in three. In the first class, the network serves as an inverse operator that learns from large pools of supervised data to map projection lines (sinogram) back to image domain [16], [17]. These methods completely neglect any geometric knowledge of the problem and solely rely on the network and rich datasets to learn the underlying physics, which can be challenging for many inverse problems. In the second category of DL-based reconstruction methods, the geometry of the problem is taken into account [18]. A plethora of recent methods deploy DL models to denoise initial FBP reconstructed images [19]–[26]. DL-based completion or denoising of the sinograms in a low-dose computed tomography (CT) setting is also proposed in [27], [28]. The third category combines solving the optimization formulation of tomographic reconstruction along the gradient descent updates with machine learning components [29]–[31]. Also, deep image priors [32] which benefit from the implicit prior offered by deep network architectures are recently adopted for tomographic reconstruction tasks [33], [34]. While in the second and third categories the knowledge of the tomographic forward model is not ignored, they still heavily rely on the knowledge of the projection angles which might not be always available. However, here we address a regime where neither these projection angles nor their underlying probability distribution are known in advance.

A. Contributions

In this paper, we present an unsupervised adversarial learning based approach for tomographic reconstruction with unknown projection angles, namely *UVTomo-GAN*. Unlike previous DL-based methods targeting the tomographic reconstruction problem, we assume that the projection angles are unknown. Furthermore, our approach does not require large

Thanks to NSF DMS-1854791, NSF OAC-1934757, and Alfred P. Sloan Foundation for funding.

M. Zehni and Z. Zhao are with the Department of Electrical and Computer Engineering and Coordinated Science Laboratory, University of Illinois at Urbana-Champaign, Urbana, IL 61801 USA (e-mail: mzehni2@illinois.edu; zhizhenz@illinois.edu).

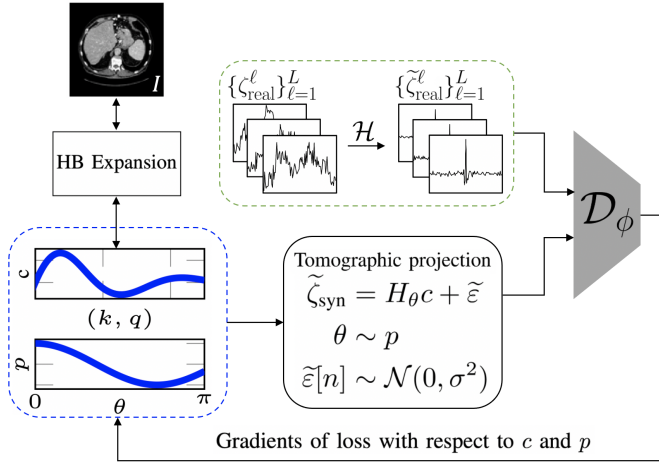


Fig. 1: An illustration of our pipeline for adversarial learning based unknown view tomography reconstruction: Given the projection lines $\{\zeta_{\text{real}}^{\ell}\}_{\ell=1}^L$ (green dashed box), we recover the truncated Hartley-Bessel expansion coefficients c of the image and projection distribution p (blue dashed box).

paired training sets and reconstructs an image given merely its tomographic measurements. Employing generative adversarial networks (GAN) [35], our approach recovers the image and projection angle distribution through matching the distributions of the generated projection lines with the measurements. Our proposed method is inspired by CryoGAN [36] in which a 3D cryo-electron microscopy (cryo-EM) map is reconstructed given a large set of noisy projections. As opposed to CryoGAN, we consider a more challenging and realistic setting in which the projection angle distribution is not known a-priori, analogous to a cryo-EM set-up. Hence, we find the projection distribution alongside the 2D image.

To recover the projection angle distribution in a GAN framework, we argue that the original generator’s loss involves sampling from the projection angles distribution which is non-differentiable. To enable the flow of gradients in the backward pass through this non-differentiable operator, we alter the training loss at the generator side using Gumbel-Softmax approximation of samples from a categorical distribution [37]. Our proposed idea is general and applicable to a vast range of similar inverse problems such as [38].

Furthermore, we adopt Hartley domain representation of the image expanded on a Hartley-Bessel (HB) basis in our reconstruction pipeline. Not only this truncated expansion represents a large class of images accurately, it also allows for the direct use of central slice theorem to generate the projection lines efficiently. We will show that this leads to a reduced computational cost in the projection line generation step. Furthermore, through use of Hartley rather than Fourier transform, we avoid handling complex values while still benefiting from Fourier related representation [39]. Our theoretical analysis and simulation results affirm the ability of our method in recovering the image and projection distribution accurately from both clean and noisy measurements.

The organization of this paper is as follows. We introduce the projection formation model and the reconstruction method in sections II and III. The analysis and experimental results

are presented in IV and V. We conclude the paper in VI.

II. PROJECTION FORMATION MODEL

We define the X-ray CT forward model as,

$$\zeta_{\ell} = \mathcal{P}_{\theta_{\ell}} I + \varepsilon_{\ell}, \ell \in \{1, 2, \dots, L\} \quad (1)$$

where $I : \mathbb{B}_2 \rightarrow \mathbb{R}_1$ is an unknown 2D compactly supported image in the unit ball \mathbb{B}_2 we wish to estimate. We restrict I to the space of absolute and square integrable functions on \mathbb{B}_2 , i.e., $I \in \mathcal{L}_1(\mathbb{B}_2) \cap \mathcal{L}_2(\mathbb{B}_2)$. \mathcal{P}_{θ} denotes the tomographic projection operator that takes the line integral along the direction specified by projection angle $\theta \in [0, \pi]$,

$$(\mathcal{P}_{\theta} I)(x) = \int_{-\infty}^{\infty} I(R_{\theta} \mathbf{x}) dy \quad (2)$$

where $\mathbf{x} = [x, y]^T$ represents the 2D Cartesian coordinates. R_{θ} is a 2×2 rotation matrix associated with θ . As I is compactly supported in \mathbb{B}_2 , its projection along any direction would also be compactly supported in the unit ball, i.e., $\mathcal{P}_{\theta} I \in \mathcal{L}_1(\mathbb{B}_1) \cap \mathcal{L}_2(\mathbb{B}_1)$. We presume the projection angles $\{\theta_{\ell}\}_{\ell=1}^L$ are unknown and randomly drawn from an *unknown* distribution p . Finally, the discretized projection lines of length m are corrupted by additive white Gaussian noise ε_{ℓ} with zero mean and variance σ^2 . Here we consider σ to be known, although an unbiased estimator of σ is attainable from the variance of the projection lines

In this paper, given a large set of noisy projection lines, i.e., $\{\zeta_{\ell}\}_{\ell=1}^L$, we aim to recover the image I and the unknown distribution of the projection angles p .

III. METHOD

A. Image Representation

To alleviate the computational cost of generating projection lines in practice, (1) is evaluated in Fourier domain using non-uniform fast Fourier transform [40] according to central slice theorem (CST). CST states that the Fourier transform of the projection line corresponds to the central slice in the 2D Fourier domain,

$$\mathcal{F}(\mathcal{P}_{\theta} I)(\xi) = \mathcal{F}(I)(\xi, \theta). \quad (3)$$

with \mathcal{F} denoting the Fourier transform and (ξ, θ) the polar coordinates. This motivates us to directly adopt CST to generate the projection lines. Therefore, in our pipeline we seek to recover the image in Fourier domain rather than pixel domain.

Since we will use the auto-differentiation in neural network optimization detailed in Section III-B, it is more convenient to keep all the variables in real values and avoid dealing with complex numbers [39]. Therefore, we use the Hartley transform of the images, which is a real representation closely related to Fourier transform and defined as:

$$\mathcal{H}(I) = \text{real}\{\mathcal{F}(I)\} - \text{imag}\{\mathcal{F}(I)\}, \quad (4)$$

where \mathcal{H} denotes the Hartley transform. We assume the image I has essential bandlimit $0 \leq s \leq \frac{1}{2}$ and is concentrated in the spatial domain with radius $R \leq \frac{m}{2}$. Therefore, $\mathcal{H}(I)$ can be expanded on an orthonormal basis on a disk of radius s . Based on the Fourier-Bessel basis introduced in [41], we construct the

real-valued steerable Hartley-Bessel (HB) basis $u_s^{k,q}(\xi, \theta) = J_s^{k,q}(\xi) \text{cas}(k\theta)$ with radial functions

$$J_s^{k,q}(\xi) = \begin{cases} N_{k,q} J_k \left(R_{k,q} \frac{\xi}{s} \right), & \xi \leq s, \\ 0, & \xi > s, \end{cases} \quad (5)$$

where J_k is the Bessel function of the first kind and integer order k , $R_{k,q}$ denotes the q -th root of J_k , and $N_{k,q} = (s\sqrt{\pi}|J_{k+1}(R_{k,q})|)^{-1}$ is the normalization factor. The angular part of the HB basis is $\text{cas}(k\theta) = \cos(k\theta) + \sin(k\theta)$. We can expand $\mathcal{H}(I)$ on the HB basis,

$$\mathcal{H}(I)(\xi, \theta) = \sum_{k=-\infty}^{\infty} \sum_{q=1}^{\infty} c_{k,q} J_s^{k,q}(\xi) \text{cas}(k\theta). \quad (6)$$

Note that, q and k correspond to radial and angular frequencies. We can truncate the expansion in (6) for functions that are well concentrated in real and Fourier space using a sampling criterion $R_{k,q} \leq 2\pi s R$ [41], [42]. The maximum angular frequency index is denoted by K_{\max} and the maximum radial frequency for k -th angular frequency is denoted by p_k . The expansion coefficients $c = \{c_{k,q} | \forall(k, q) \text{ s.t. } |k| \leq K_{\max}, 1 \leq q \leq p_k\}$ are the unknown parameters of I we aim to recover. For an image with $s < 0.5$ or $R < \frac{m}{2}$, c has less number of terms than the number of pixels I , i.e., the cardinality of $c < m^2$. Thus, c would constitute a compressed representation of the image.

Given the image expanded on HB basis, following CST, the Hartley transform of the projection line from angle θ_ℓ is simply obtained by setting $\theta = \theta_\ell$ in (6) and is written as:

$$\mathcal{H}(\mathcal{P}_{\theta_\ell} I)(\xi) = \sum_{k=-K_{\max}}^{K_{\max}} \sum_{q=1}^{p_k} c_{k,q} J_s^{k,q}(\xi) \text{cas}(k\theta_\ell) = H_{\theta_\ell}(\xi) c. \quad (7)$$

Therefore, we rewrite (1) in Hartley domain as:

$$\tilde{\zeta}_\ell = H_{\theta_\ell} c + \tilde{\varepsilon}_\ell, \quad \theta_\ell \sim p, \quad \ell \in \{1, 2, \dots, L\}, \quad (8)$$

with $\tilde{\zeta} = \mathcal{H}(\zeta)$ and $\tilde{\varepsilon} = \mathcal{H}(\varepsilon)$. The Hartley transform is unitary due to its self-adjoint and self-inverse properties. Therefore, the distribution of the Gaussian additive noise is preserved after taking the Hartley transform, i.e., $\tilde{\varepsilon}_\ell \sim \mathcal{N}(\mathbf{0}_m, \sigma^2 I_m)$ where $\mathbf{0}_m$ is a vector of zeros of length m and I_m is an $m \times m$ identity matrix.

The Fourier-Bessel (FB) expansion coefficients a of $\mathcal{F}(I)$ are related with c by

$$a_{k,q} = \begin{cases} \frac{1}{2}(c_{k,q} + c_{-k,q}) + \frac{i}{2}(-c_{k,q} + c_{-k,q}) & k \text{ even}, \\ \frac{1}{2}(-c_{k,q} + c_{-k,q}) - \frac{i}{2}(c_{k,q} + c_{-k,q}) & k \text{ odd}. \end{cases} \quad (9)$$

The images can be reconstructed from a following the closed form expression in [41]:

$$I(r, \varphi) = \sum_{k=-K_{\max}}^{K_{\max}} \sum_{q=1}^{p_k} a_{k,q} \psi_s^{k,q}(r, \varphi), \quad (10)$$

where

$$\psi_s^{k,q}(r, \varphi) = \frac{2s\sqrt{\pi}(-1)^q R_{k,q} J_k(2\pi sr)}{i^k((2\pi sr)^2 - R_{k,q}^2)} e^{ik\varphi}, \quad (11)$$

is the 2D inverse Fourier transform of the Fourier-Bessel function with (r, φ) denoting the polar coordinates in spatial domain. Since we have the analytical form of the basis function, we can easily evaluate the function values on Cartesian coordinates $[x, y]$ with $x = r \cos \varphi$ and $y = r \sin \varphi$.

B. Adversarial learning for reconstruction

Our reconstruction criterion is matching the distribution of the real projection dataset and the projection lines generated by c and p following (8). As GANs have proven suitable for matching a target distribution, we employ an adversarial learning framework presented in Fig. 1.

Our adversarial learning approach consists of a critic (discriminator) \mathcal{D}_ϕ and a generator \mathcal{G} . Unlike classic GAN models with generators parameterized by neural networks with learnable weights, we specify the generator \mathcal{G} by the known projection model defined in (8), the parameters of the image and projection angle distribution, i.e., c and p . The generator's goal is to output projection lines that are close to the real projection dataset $\{\tilde{\zeta}_{\text{real}}^\ell\}_{\ell=1}^L$ in distribution and hence fool the critic. For our model, the unknowns we seek to estimate at the generator side are c and p . On the other hand, the discriminator \mathcal{D}_ϕ , parameterized by ϕ , tries to distinguish between the observations and the generated projections. Our pipeline is depicted in Fig. 1.

We use Wasserstein GAN [43] loss with gradient term (WGAN-GP) [44]. We express the loss function in terms of c , p and ϕ and the min-max problem as,

$$\mathcal{L}(c, p, \phi) = \sum_{b=1}^B \mathcal{D}_\phi(\tilde{\zeta}_{\text{real}}^b) - \mathcal{D}_\phi(\tilde{\zeta}_{\text{syn}}^b) + \lambda \left(\left\| \nabla_{\tilde{\zeta}} \mathcal{D}_\phi(\tilde{\zeta}_{\text{int}}^b) \right\| - 1 \right)^2 \quad (12)$$

$$\hat{c}, \hat{p} = \underset{c, p}{\text{argmin}} \max_{\phi} \mathcal{L}(c, p, \phi), \quad (13)$$

where \mathcal{L} denotes the loss, B and b represent the batch size and the index of a sample in the mini-batch, respectively. Also, $\tilde{\zeta}_{\text{real}}$ and $\tilde{\zeta}_{\text{syn}}$ mark the real and synthesized projections in Hartley domain. $\tilde{\zeta}_{\text{syn}}$ is generated from the estimated image \hat{c} and projection distribution \hat{p} following $\tilde{\zeta}_{\text{syn}} = H_{\theta} \hat{c} + \tilde{\varepsilon}$, $\theta \sim \hat{p}$. Note that the last term in (12) is the gradient penalty with weight λ and roots from the Lipschitz continuity constraint of the critic in a WGAN setup. We use $\tilde{\zeta}_{\text{int}}$ to denote a linearly interpolated sample between a real and a synthetic projection line, i.e., $\tilde{\zeta}_{\text{int}} = \alpha \tilde{\zeta}_{\text{real}} + (1-\alpha) \tilde{\zeta}_{\text{syn}}$, $\alpha \sim \text{Unif}(0, 1)$. In our experiments, we also used spectral normalization (SN) [45] and found that SN is a sufficient replacement for the gradient penalty term in terms of stabilizing the training. Thus, we set $\lambda = 0$ in (12) and only use spectral normalization to regularize the critic. Following common practice, we solve (13) by alternating updates between ϕ and the generator's variables, i.e., c and p , based on the associated gradients.

The loss at the generator side for a fixed \mathcal{D}_ϕ is,

$$\mathcal{L}_G(c, p) = - \sum_{b=1}^B \mathcal{D}_\phi(H_{\theta_b} c + \tilde{\varepsilon}_b), \quad \theta_b \sim p. \quad (14)$$

While (14) is differentiable with respect to c , its gradient of p is not defined, as it involves sampling θ_b from the distribution p . This hinders updating p through gradient back-propagation. To address this, we aim to design an alternative approximation of (14) which is differentiable with respect to p .

To accommodate this approximation, we first discretize the support of the projection angles, i.e., $[0, \pi]$, uniformly into N_θ bins. This makes p a probability mass function (PMF) of

Algorithm 1 UVTomo-GAN

Require: $\alpha_\phi, \alpha_c, \alpha_p$: learning rates for ϕ, c and p . n_{disc} : the number of iterations of the critic per generator iteration.

Input: $\{\tilde{\zeta}_\ell^{\text{real}}\}_{\ell=1}^L$. Random initialization of c . The distribution p is initialized with $\text{Unif}(0, \pi)$.

Output: Estimates of I and p .

- 1: **while** ϕ has not converged **do**
 - 2: **for** $t = 0, \dots, n_{\text{disc}} - 1$ **do**
 - 3: Sample a batch from real data, $\{\tilde{\zeta}_{\text{real}}^b\}_{b=1}^B$
 - 4: Sample a batch of simulated projections using estimated c and p , i.e. $\{\tilde{\zeta}_{\text{syn}}^b\}_{b=1}^B$ following (8)
 - 5: Generate interpolated samples $\{\tilde{\zeta}_{\text{int}}^b\}_{b=1}^B$, $\tilde{\zeta}_{\text{int}}^b = \alpha \tilde{\zeta}_{\text{real}}^b + (1 - \alpha) \tilde{\zeta}_{\text{syn}}^b$ with $\alpha \sim \text{Unif}(0, 1)$
 - 6: Update the discriminator using gradient ascent steps using the gradient of (12) with respect to ϕ .
 - 7: **end for**
 - 8: Sample a batch of $\{r_{i,b}\}_{b=1}^B$ using (18)
 - 9: Update c and p using stochastic gradient descent steps by taking the gradients of (19) with respect to c and p .
 - 10: **end while**
-

length N_θ with the following properties:

$$\sum_{i=1}^{N_\theta} p_i = 1, \text{ and } p_i \geq 0, \forall i \in \{1, \dots, N_\theta\}. \quad (15)$$

Now p corresponds to a discrete or categorical distribution over θ , which implies the sampled projection angles from p can only belong to N_θ discrete categories. Therefore, we rewrite the loss function (14) as:

$$\mathcal{L}_G(c, p) = - \sum_{b=1}^B \sum_{t=1}^{N_\theta} \delta(\theta_t - \theta_b) \mathcal{D}_\phi(H_{\theta_t} c + \tilde{\varepsilon}_b), \theta_b \sim p. \quad (16)$$

A closer look at (16) reveals that $\delta(\theta_t - \theta_b)$, $\theta_b \sim p$ is a sample from the discrete distribution p . This enables us to incorporate the notion of Gumbel-Softmax distribution and approximate (14) as:

$$\mathcal{L}_G(c, p) \approx - \sum_{b=1}^B \sum_{i=1}^{N_\theta} r_{i,b} \mathcal{D}_\phi(H_{\theta_i} c + \tilde{\varepsilon}_b), \quad (17)$$

with

$$r_{i,b} = \frac{\exp((g_{b,i} + \log(p_i))/\tau)}{\sum_{j=1}^{N_\theta} \exp((g_{b,j} + \log(p_j))/\tau)}, g_{b,i} \sim \text{Gumbel}(0, 1) \quad (18)$$

where τ is the softmax temperature factor. As $\tau \rightarrow 0$, $r_{i,b} \rightarrow \text{one-hot}(\arg\max_i [g_{b,i} + \log(p_i)])$. Moreover, to obtain samples from the Gumbel(0, 1) distribution, it suffices to draw $u \sim \text{Unif}(0, 1)$, $g = -\log(-\log(u))$ [37]. Note that due to the reparametrization trick applied in (17), the approximated generator's loss has a tangible gradient with respect to p .

We also add prior knowledge on the image and projection distribution in the form of regularization terms. Hence, the regularized loss function we optimize at the generator side is:

$$\mathcal{L}(c, p) = \mathcal{L}_G(c, p) + \gamma_1 \text{gTV}(c) + \gamma_2 \|c\|^2 + \gamma_3 \text{TV}(p) + \gamma_4 \|p\|^2 \quad (19)$$

where we include total variation (TV) and ℓ_2 regularization

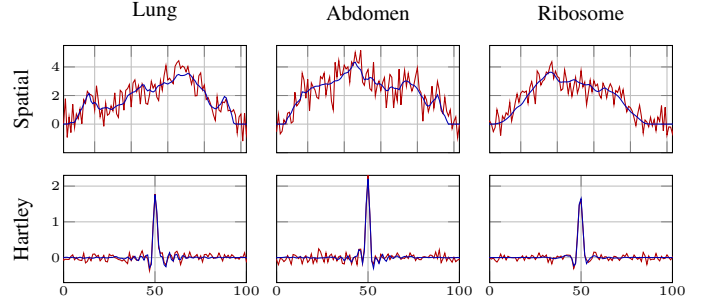


Fig. 2: Samples of clean (blue) and noisy (red) projection lines in spatial (first row) and Hartely (second row) domain. For noisy data SNR = 3.

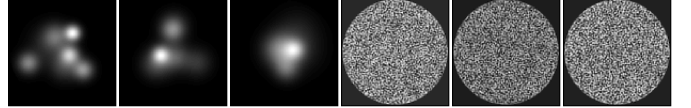


Fig. 3: Examples of the initialization images used for EM baselines.

terms for the image, with γ_1 and γ_2 weights. To construct the TV of the image in terms of c , we use (9)-(10) to render I on a Cartesian grid in spatial domain and then compute total variation of I . Furthermore, we assume that the unknown PMF is a piece-wise smooth function of projection angles (which is a valid assumption especially in single particle analysis in cryo-electron microscopy [46]), therefore adding TV and ℓ_2 regularization terms for the PMF with γ_3 and γ_4 weights. We present the pseudo-code for UVTomo-GAN in Alg. 1.

C. Maximum Marginalized Likelihood Estimation via Expectation-Maximization

As a baseline for UVTomo-GAN, we consider maximum marginalized likelihood estimation (MMLE). We solve MMLE in Fourier domain via expectation-maximization (EM) and represent $\mathcal{F}(I)$ with its expansion coefficients a on Fourier-Bessel bases. Thus, MMLE is formulated as

$$\hat{a}, \hat{p} = \underset{a, p}{\text{argmax}} \sum_{\ell=1}^L \log \left(\sum_{i=1}^{N_\theta} P(\mathcal{F}(\zeta_\ell) | a, \theta_i) p_i \right). \quad (20)$$

To solve (20), we take the gradients with respect to a and p and set them to zero. For p , we further impose $\sum_{i=1}^{N_\theta} p_i = 1$. This yields the following alternating updates for a and p , in the form of:

$$\text{(E-step)} : r_{i,j}^t = \frac{\exp \left(-\frac{\|\mathcal{F}(\zeta_i) - H_{\theta_j} a^{t-1}\|^2}{2\sigma^2} \right)}{\sum_{j=1}^{N_\theta} p_j^{t-1} \exp \left(-\frac{\|\mathcal{F}(\zeta_i) - H_{\theta_j} a^{t-1}\|^2}{2\sigma^2} \right)}, \quad (21)$$

$$\text{(M-step)} : \begin{cases} a^t = \underset{a}{\text{argmin}} \|\mathbf{H}^t a - \mathbf{y}^t\|^2, \\ p_j^t = \frac{\sum_{i=1}^L r_{i,j}^t}{\sum_{i=1}^L \sum_{j=1}^{N_\theta} r_{i,j}^t}, \end{cases} \quad (22)$$

and

$$\{\mathbf{H}^t a\}(\xi, \theta) = \sum_{i=1}^L \sum_{j=1}^{N_\theta} r_{i,j}^t a_{k,q} J_s^{k,q}(\xi) e^{ik\theta_j} \delta(\theta - \theta_j), \quad (23)$$

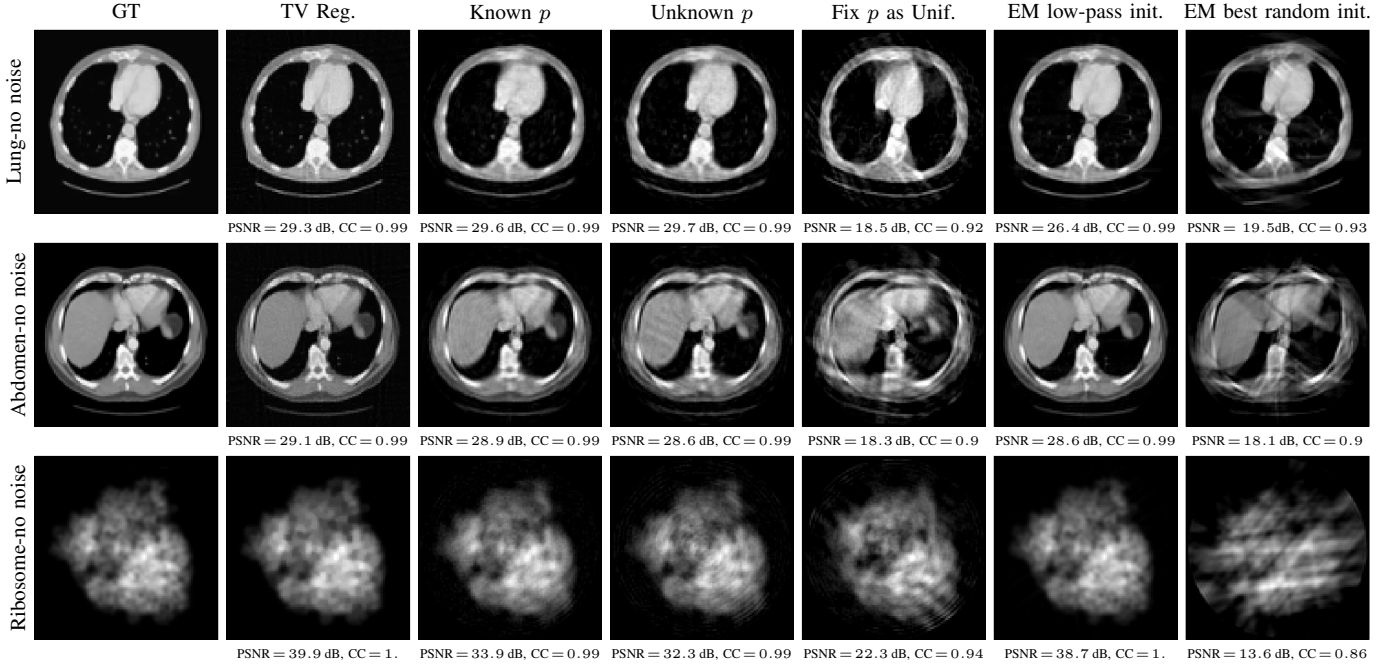


Fig. 4: Visual comparison of UVTomo-GAN with different baselines in no noise setting, i.e. $\text{SNR} = \infty$. The description of the columns: 1) ground truth image (GT), 2) TV-regularized reconstruction with known projection angles, 3) UVTomo-GAN with known p , 4) UVTomo-GAN with unknown p , 5) UVTomo-GAN with unknown p but assumed to be a uniform distribution, 6) EM initialized with low-pass filtered GT image, 7) EM with random initialization. The PSNR and CC, comparing the reconstructed images and the GT are also provided underneath each image.

$$\mathbf{y}^t(\xi, \theta) = \begin{cases} \sum_{i=1}^L \sum_{j=1}^{N_\theta} r_{i,j}^t \mathcal{F}(\zeta_i)(\xi) \delta(\theta - \theta_j) & \theta \in [0, \pi), \\ \sum_{i=1}^L \sum_{j=1}^{N_\theta} r_{i,j}^t \mathcal{F}(\zeta_i)(-\xi) \delta(\theta - \pi - \theta_j) & \theta \in [\pi, 2\pi), \end{cases} \quad (24)$$

where $r_{i,j}$ denotes the probability that the i -th projection line is associated with θ_j angle and t is the iteration index. Also, $H_\theta a$ generates the projection line at θ direction in Fourier domain given FB expansion coefficients a . In (21)-(22), we update the probabilistic angular assignments for the projection lines in the E-step while updating a and p in the M-step. Note that, in the absence of noise, i.e., $\sigma = 0$, the E-step reduces to template matching [47].

Our choice of FB expansion for the image has a two-fold advantage: 1) it acts as an implicit regularizer that confines the space of reconstructed images to the span of truncated FB bases, 2) updating a at step t in the M-step is equivalent to projecting \mathbf{y}^t on the truncated FB bases. This can be done efficiently as discussed in [41]. Thus, using this representation significantly reduces the computational complexity of the M-step. The updates on a at iteration t take the following form:

$$a_{k,q}^t = \sum_{\ell=1}^{n_\xi} \sum_{j=1}^{N_\theta} \sum_{i=1}^L \frac{1}{b_j^t} \mathbf{y}^t(\xi_\ell, \theta_j) e^{-ik\theta_j} J_s^{k,q}(\xi_\ell) \xi_\ell w(\xi_\ell), \quad (25)$$

where $b_j^t = \sum_{i=1}^L r_{i,j}^t$, ξ_ℓ and $w(\xi_\ell)$ are the associated quadrature points and weights for numerical integration. Following [41], we keep $n_\xi = 4cR$.

D. Computational complexity

We conclude this section by comparing the computational complexity per iteration of UVTomo-GAN and EM.

UVTomo-GAN Complexity: Based on Algorithm 1, we split the computational cost of UVTomo-GAN between: 1) the critic and 2) the generator (i.e., c and p) updates. Let $C_{\mathcal{D}}$ denote a fixed computational cost related to forward and backpropagation passes through the critic \mathcal{D}_ϕ . As expected, $C_{\mathcal{D}}$ depends on the batch size, network architecture and the size of its input. Thus, the larger the discriminator network, the higher the $C_{\mathcal{D}}$. For our critic architecture, we use a cascade of $N \ll m$ fully connected (FC) layers with intermediate ReLU non-linearities. Therefore, $C_{\mathcal{D}}$ points to the cost of matrix multiplication and backward passes through these N layers. Furthermore, we keep the input and output sizes of these FC layers to be $O(m)$ (m is the image/projection size). Therefore, $C_{\mathcal{D}} = O(m^2 N) = O(m^2)$. As these operations can be parallelized on GPU, forward and backward passes through \mathcal{D}_ϕ are time-efficient. For batch size $B = O(m)$, the cost of discriminator update is $O(B C_{\mathcal{D}}) = O(m^3)$.

For updating the generator according to (17), first we generate $N_\theta = O(m)$ projection lines or templates. This is done in $O(m^3)$. A thorough discussion on the derivation of this computational complexity term is deferred to Appendix VII-A. In the naive form, if the projection operator is implemented with a matrix in spatial domain, then the template generation step would cost $O(m^4)$. Thus, HB representation leads to $O(m)$ improvement in the template generation step.

In our implementation of (17), instead of using B different

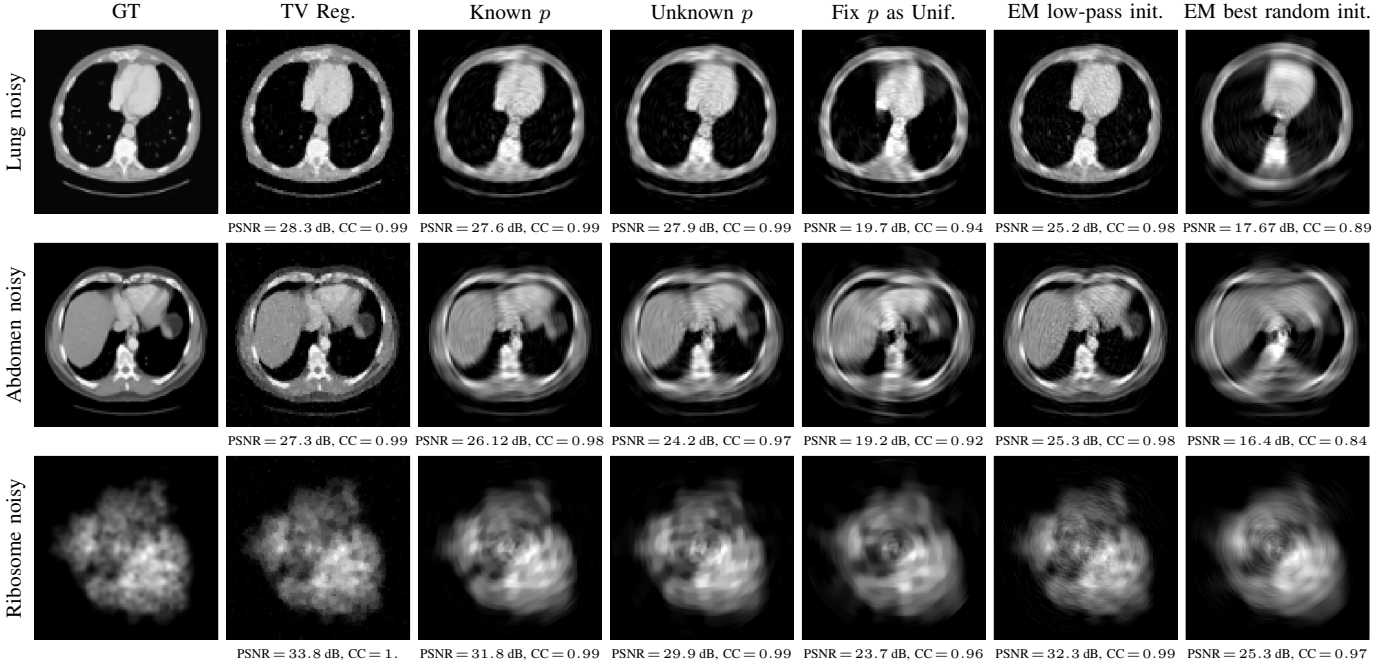


Fig. 5: Visual comparison of UVTomo-GAN with different baselines in noisy setting, i.e., SNR = 3. Examples of noisy projection lines for this experiment are plotted in Fig. 2. The description of the columns: 1) ground truth image (GT), 2) TV-regularized reconstruction with known projection angles, 3) UVTomo-GAN with known p , 4) UVTomo-GAN with unknown p , 5) UVTomo-GAN with unknown p but assumed to be a uniform distribution, 6) EM initialized with low-pass filtered GT image, 7) EM with random initialization. The PSNR and CC, comparing the reconstructed images and the GT are also provided underneath each image.

noise realizations $\{\tilde{\varepsilon}_b\}_{b=1}^B$ for each of the clean templates, we consider N_θ noisy templates in total. This means the loss function we use at the generator side is:

$$\mathcal{L}_G(c, p) \approx - \sum_{b=1}^B \sum_{i=1}^{N_\theta} r_{i,b} \mathcal{D}_\phi(H_{\theta_i} c + \varepsilon_i). \quad (26)$$

Indeed in the absence of noise, (26) matches (17). However, in the noisy case, the benefits of (26) are two-fold: 1) having the same performance as (17) empirically, 2) reducing the number of passes through the discriminator.

Consequently, adding up the cost of passing N_θ projection templates through \mathcal{D}_ϕ leads to a total computational cost of $O(m^3 + mC_{\mathcal{D}})$ per generator update step. We update c and p every n_{disc} iterations. Therefore, the average cost of UVTomo-GAN per iteration including the generator and critic's updates is $O(\frac{(n_{\text{disc}}-1)m^3 + (m^3 + mC_{\mathcal{D}})}{n_{\text{disc}}}) = O(m^3)$.

EM Complexity: For EM, we specify the computational cost of E-step and M-step. At each E-step, we generate N_θ projection templates. If these templates are generated following CST and using the non-uniform Fourier transform of the image, they require $O(m^2 \log m)$ computations. Next, we update the angular assignments of $L \gg m$ projection lines by comparing them against $O(m)$ templates, hence a cost of $O(m^2 L)$. Then, the total cost of E-step is $O(m^2 \log m + m^2 L) = O(m^2 L)$. For the M-step, computing \mathbf{y}^t from the projection lines costs $O(mL)$ while updating FB coefficients a in (25) requires $O(m^3)$ or $O(m^2 \log m)$ using fast Bessel transform [41]. Finally, the overall computational complexity for EM is

$O(m^3 + m^2 L)$. Note that, the cost of naive implementation of M-step in pixel domain with projection operators implemented as finite sized matrices would be $O(m^4)$. Therefore, Fourier domain implementation alongside FB representation of the image improves M-step computationally by $O(m)$. While, other implementations of M-step using convolution are feasible [48], [49], it is not the focus of our work.

Notice that EM has a higher per-iteration computational cost compared to UVTomo-GAN as $L \gg m$. For example in our experiments, we have $m = 101$ and $L = 2 \times 10^4$, thus $L \approx O(m^2)$. Empirically, we observe that UVTomo-GAN requires more iterations to converge. We attribute this to the difference between the convergences of stochastic gradient descent used in UVTomo-GAN versus full batch processing in EM. On the other hand, we show that while UVTomo-GAN is robust to the choice of initialization, EM is highly likely to get stuck in a bad local solution with random initialization. This observation is also reported in cryo-EM settings in [46], [50].

IV. ANALYSIS

In this section, we first define our notations and then formally state the reconstruction guarantees of UVTomo-GAN.

A. Notations

We assume the image $f \in \mathcal{L}_1(\mathbb{B}_2) \cap \mathcal{L}_2(\mathbb{B}_2)$ has a bandlimit $0 < s \leq 0.5$ and compactly supported in the unit ball \mathbb{B}_2 . In addition, $f \in \text{span}\{\psi_{k,q}^s\}_\Omega$, $\Omega = \{(k, q) \mid |k| \leq K_{\text{max}}, 1 \leq q \leq$

$p_k\}$ with $\psi_{k,q}^s$ defined in (10). Thus, the Hartley transform of f is expanded on a HB basis set. A measurement ζ associated with the projection angle $\theta \sim p$ is $\zeta = \mathcal{P}_\theta f + \varepsilon$ with $\varepsilon[n] \sim q_\varepsilon$ denoting additive IID noise. We assume q_ε has full support in Fourier domain, i.e., $\{\mathcal{F}q_\varepsilon\}(\omega) \neq 0, \forall \omega$.

Let $O(2)$ denote the group of all possible rotations and reflections, i.e., $\Gamma^T \Gamma = I$ and $\det(\Gamma) = \pm 1, \forall \Gamma \in O(2)$. The action of the $O(2)$ group on f is defined as,

$$(\Gamma f)(\mathbf{x}) = f(\Gamma^{-1} \mathbf{x}), \forall \Gamma \in O(2) \quad (27)$$

where $\mathbf{x} = [x, y]$ denotes the Cartesian coordinate. On the other hand, the action of Γ on a probability distribution p defined over $[0, \pi]$ manifests as a combination of flip or circular shift. The group $O(2)$ partitions the space of $\text{span}\{\psi_{k,q}^s\}_\Omega$ into a set of equivalence classes where $[f] = \{\Gamma f, \forall \Gamma \in O(2)\}$. Let $P_{f,p}^{\text{clean}}$ and $P_{f,p}^{\text{noisy}}$ denote the probability distributions induced by clean and noisy projections, i.e., $\zeta_{\text{clean}} = \mathcal{P}_\theta f$ and $\zeta_{\text{noisy}} = \mathcal{P}_\theta f + \varepsilon$ with $\theta \sim p$, respectively.

B. Theoretical results

Here we elaborate upon the theoretical reconstruction guarantees for our proposed method.

Theorem 1: Consider $f, g \in \mathcal{L}_1(\mathbb{B}_2) \cap \mathcal{L}_2(\mathbb{B}_2)$ and the associated bounded probability distributions p_f and p_g on the projection angles distributed in $[0, \pi]$. Then,

$$P_{f,p}^{\text{clean}} = P_{g,p_g}^{\text{clean}} \Rightarrow [f] = [g], [p_f] = [p_g]. \quad (28)$$

Furthermore, if $f = \Gamma g, \Gamma \in O(2)$, then $p_f = \Gamma p_g$.

The proof is provided in Appendix VII-B. Intuitively, Theorem 1 states that if f and g have the same induced clean projection distribution, then the underlying objects and projection distributions are equivalent up to a rotation and reflection. We link the proof of this theorem to unique angular recovery in unknown view random tomography [6], [7].

Theorem 2: Assume $f \in \mathcal{L}_1(\mathbb{B}_2) \cap \mathcal{L}_2(\mathbb{B}_2)$ denoting the ground truth (GT) image and p representing the bounded GT probability distribution over the projection angles $\theta \in [0, \pi]$. Let \hat{f} and \hat{p} stand for the recovered image and the bounded probability distribution after the convergence of UVTomo-GAN. Consider the asymptotic case as $L \rightarrow \infty$. Then,

$$P_{f,p}^{\text{noisy}} = P_{\hat{f},\hat{p}}^{\text{noisy}} \Rightarrow \hat{f} = \Gamma f, \hat{p} = \Gamma p, \quad (29)$$

for a unique $\Gamma \in O(2)$.

The proof is available in Appendix VII-C. This theorem validates that upon the convergence of UVTomo-GAN in the presence of noise and infinite number of noisy projections, the GT image and projection angle distribution is recovered up to a rotation-reflection transformation. We defer the study of sample complexity of UVTomo-GAN with finite size projection dataset to future work.

V. NUMERICAL RESULTS

A. Experiment setup

Dataset: In our experiments, to verify the generalization of our method, we use three different images. Two are biomedical images of lung and abdomen from low dose CT (LDCT) dataset [51]. For the third image, we generated the 3D map of 100S Ribosome [52] using its protein sequence in

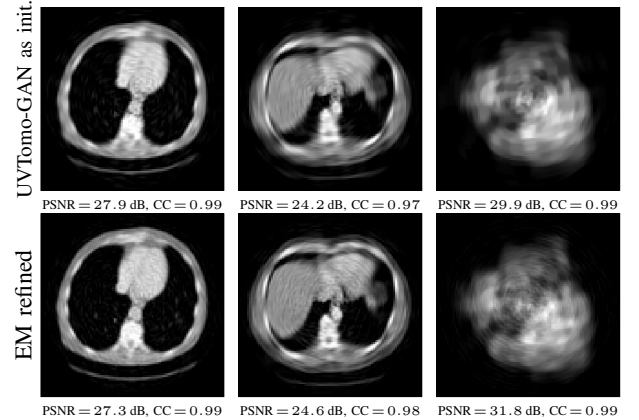


Fig. 6: Visualization of EM refined results given images reconstructed by UVTomo-GAN as an ab-initio model. PSNR and CC metrics reported before and after refinement. The experiment setup for UVTomo-GAN is the same as Fig. 5.

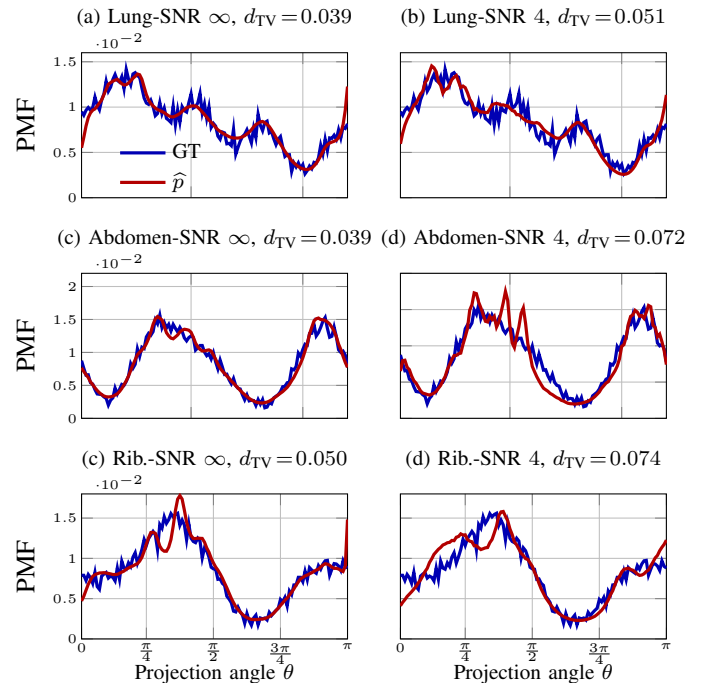


Fig. 7: Comparison between ground truth (GT) sample distribution of the projection angles (red) and the one estimated by our method \hat{p} (blue).

Chimera [53] and took a 2D projection of the generated map along a random view. We resized all images to 101×101 dimension. We refer to these images as Lung, Abdomen and Ribosome. We synthesize the real projection dataset in Hartley domain following (8) where p is a smooth probability distribution over the projection angles and is chosen randomly. To generate the real dataset, we finely discretize the projection angle domain $[0, \pi]$ with 240 equal sized bins and use non-uniform polar FFT [54] and CST to generate the projection lines. For the reconstruction, we consider a coarser grid for the projection angles with $N_\theta = 120$ bins. This way we are taking into account the approximated discretization of θ at the reconstruction time which might differ from how the real

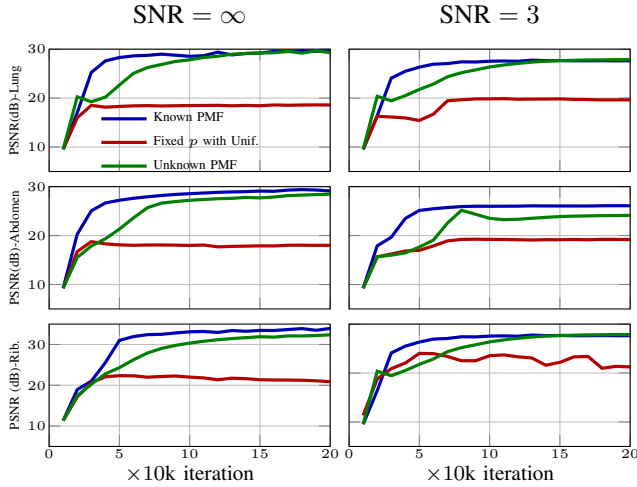


Fig. 8: Convergence results for the no noise ($\text{SNR} = \infty$) and noisy ($\text{SNR} = 3$) experiments. We compare UVTomo-GAN with unknown p (green curve) versus GAN-based baselines with known p (red) and fixed p with uniform distribution (blue). Vertical axis shows the PSNR in dB and the horizontal axis is the training iteration number.

projection angles are obtained. We study two noise regimes: 1) no noise, $\text{SNR} = \infty$ and 2) noisy with $\text{SNR} = 3$, SNR denoting the ratio of signal-to-noise power of the projection lines:

$$\text{SNR} = \frac{\mathbb{E}\{\|\zeta_{\text{clean}}\|^2\}}{\mathbb{E}\{\|\zeta_{\text{noisy}} - \zeta_{\text{clean}}\|^2\}} \quad (30)$$

where ζ_{clean} and ζ_{noisy} stand for the clean and noisy projection lines in spatial domain, respectively. Examples of clean and noisy projection lines in both spatial and Hartley domains are illustrated in Fig. 2. In all our experiments, the number of projection lines is $L = 2 \times 10^4$.

Training and Network Architecture: We set a batch-size of $B = 100$. We have separate learning rates for \mathcal{D}_ϕ , c and p denoted by α_ϕ , α_c and α_p , but often choose $\alpha_\phi = \alpha_c$. We have a cosine and step decay schedule for no noise and noisy experiments. We update \mathcal{D}_ϕ , c and p using stochastic gradient descent (SGD) steps. We clip the gradients of \mathcal{D}_ϕ and c by 1 and 10 respectively and normalize the gradients of p to have norm 0.1. We train the discriminator $n_{\text{disc}} = 4$ times per updates of c and p . Although, after training for a while, we increase the frequency of updating c and p by setting $n_{\text{disc}} = 2$. Once converged, we use the reconstructed HB expansion coefficients to re-render the image in spatial domain according to (9)-(10).

Our architecture of the discriminator consists of four fully connected (FC) layers with ℓ , $\ell/2$, $\ell/4$, and 1 output sizes with ReLU [55] activations in between. We choose $\ell = 512$ for no noise and $\ell = 256$ for noisy experiments. Our justification for adopting a smaller discriminator network in noisy case is to avoid overfitting to noisy projections and reduce the leak of noise in the final reconstruction. In addition, we choose a constant weight for the Tikonov regularization for all (k, q) . However, in the noisy case, we use a weight decay that increases for higher frequencies, i.e., larger (k, q) s. We found this helpful in further suppressing the noisy leaking into high

frequency components of the reconstruction.

To improve the stability of the GAN training, we use spectral normalization [45], applied to all discriminator layers. To enforce p to have non-negative values while summing up to one, we set it to be the output of a Softmax layer. To check the robustness of UVTomo-GAN with respect to initialization, in our experiments we try two initialization schemes for c : 1) initialize each entry of c independently with a random variable drawn from $\mathcal{N}(0, 4 \times 10^{-4})$, 2) $c_{0,0} = 0.01$ and $c_{k,q} = 0, \forall k, q$. In this draft we only report the results of the first initialization scheme as both led to similar results. We set p to be a uniform distribution initially. For the critic, we randomly initialize the weights of the FC layers with a zero-mean Gaussian distribution and standard deviation 0.05 and set the biases to zero. Our implementation is in PyTorch and runs on single GPU.

Evaluation metrics: To assess the quality of the reconstructed image, we use peak signal to noise ratio (PSNR) and normalized cross correlation (CC). Higher value of these metrics signals better quality of the reconstruction. Also, to evaluate \hat{p} compared to the ground truth, we use total variation distance (TV) defined as:

$$d_{\text{TV}} = \frac{1}{2} \|p - \hat{p}\|_1. \quad (31)$$

B. Baselines

We benchmark UVTomo-GAN with unknown p against four baselines. For the first two, we have the same GAN-based reconstruction framework as UVTomo-GAN. Although, in the first baseline we assume p is known in advance and for the second baseline, we fix p with a uniform distribution. Thus, for the GAN-based benchmarks we still follow Alg. 1. However, during training, we skip updating p and instead use the GT p and the uniform distribution.

For known projection angles $\{\theta_\ell\}_{\ell=1}^L$, we also formulate the reconstruction as a TV regularized optimization solved by ADMM [56] as our third baseline. We use the ADMM implementation in GlobalBioIm [57]. Finally, we compare against MMLE (20) solved by EM (21)-(22). Note that unlike the third baseline, in EM we do not know the projection angles. We assess two different initialization schemes for EM. In *EM low-pass init*, we utilize a low-pass filtered version of the GT image to initialize EM. For the second initialization strategy, we use 10 random initializations. We test two different forms of initializations, 1) randomly located Gaussian blobs with random standard deviations, 2) initializing each pixel with Uniform distribution, i.e., $I[x, y] \sim \text{Unif}[0, 1]$. In our experiments, we report the best results for EM out of these 10 random initializations, hence the name *EM best random init* for this baseline. Examples of the initializations used for EM baselines are provided in Fig. 3.

C. Experimental results

Quality of reconstructed image: Fig. 4-5 compare the results of UVTomo-GAN with unknown p against the GT image and the aforementioned baselines for no noise and noisy scenarios. The results of UVTomo-GAN with unknown p

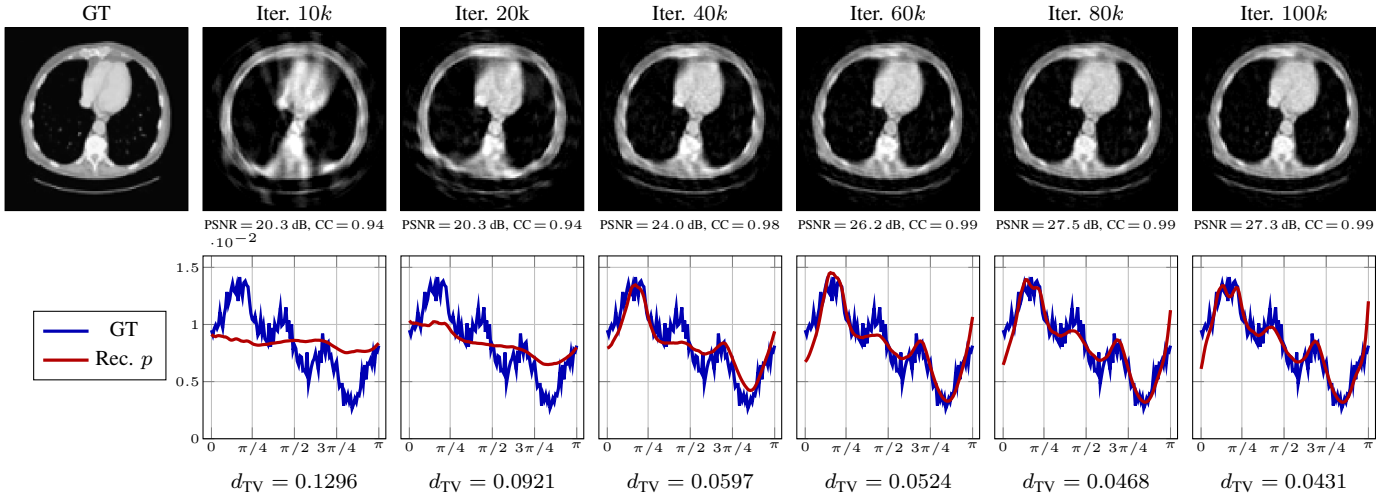


Fig. 9: Convergence of the reconstructed images and the projection distribution throughout different iterations. For each iteration, we report PSNR and CC of the reconstructed image and TV distance of recovered p . In this experiment $SNR = \infty$.

closely resembles the oracle GAN-based known p baseline, both qualitatively and quantitatively. However, with unknown p , the reconstruction problem is more challenging. Note that, although by fixing p with a Uniform distribution (fifth column in Fig. 4-5) the overall shape of the GT image emerges in the final reconstruction, the details are not successfully recovered. This highlights the importance of updating p to retrieve details accurately in the reconstruction. A similar observation, although in a different setting is reported in [58].

In addition, while the first and third baselines are performing well on the reconstruction task, they have the advantage of knowing the projection angles or their distribution. In our experiments we observe that EM is sensitive to the initialization. While EM initialized with low-pass filtered GT image converges well, EM best random init baseline fails in reconstructing the image accurately.

Fig. 5 also displays the effect of noise in the final reconstruction. We observe that the presence of noise makes the reconstruction task more challenging and degrades the reconstruction quality compared to the no noise case. This happens as the discriminator is having a harder time distinguishing signal from noise components given the noisy projections. As a refinement, we can use the UVTomo-GAN reconstruction as a good initialization for EM as shown in Fig. 6.

Quality of reconstructed p : Comparison between the GT distribution of the projection angles and the one recovered by UVTomo-GAN with unknown p is provided in Fig. 7. Note that the recovered p matches the GT distribution both visually and quantitatively in terms of TV distance. Although, the quality of the recovered PMF in the noisy cases (Fig. 7-(b), (d), (e)) is not as good as the no noise case, it still closely resembles the GT projection distribution. This proves the ability of our approach to recover p accurately under different distributions and noise regimes.

Convergence: We exhibit the convergence curves in terms of PSNR versus training iteration for no noise and noisy experiments in Fig. 8. We compare the convergence of UVTomo-

GAN for three cases, 1) known p , 2) fixed p with uniform distribution and 3) unknown p and recovered alongside the image. Note that the knowledge of p leads to a faster convergence. However as training evolves and a more accurate p is obtained, the quality of the reconstructed image for unknown p approaches the known PMF case.

Furthermore, when fixing the PMF with uniform distribution, after a certain number of iterations, we see no improvement in the reconstructed image. This is attributed to having an inaccurate PMF which hinders the correct distribution matching of synthetic and real measurements. Thus, the high frequency details in the final reconstructed image do not appear correctly (as also seen in Fig. 4-5). This once again indicates the importance of recovering p to have high quality reconstructions.

We also visualize the evolution of the reconstructed image and the projection distribution in Fig. 9 throughout different training iterations. We obtain a reasonable image and PMF at early stages of training, i.e., after 20k-40k iterations (which takes roughly 6-12 minutes). As expected, the image is further refined with more training iterations.

VI. CONCLUSION

In this paper, we proposed an adversarial learning approach for the unknown view tomographic reconstruction problem. We presumed the projection angles and the probability distribution they are drawn from are not known a-priori. Thus, we recovered both the unknown image and probability distribution of the projection angles via a distribution matching formulation solved through a min-max game between a critic and a generator. To further reduce computational burdens, we employed a Fourier related representation of the image, expanded on a Hartley-bessel basis set. For the GAN training, we showed that the loss function at the generator side is non-differentiable with respect to the projection angle distribution. Thus, we used the Gumbel-Softmax approximation of samples from discrete distributions. We studied the theoretical guarantees of

UVTomo-GAN and demonstrated that asymptotically unique recovery of the image and projection distribution is achieved. Our simulation results confirmed the capability of our method in accurate image and projection distribution recovery under different noise regimes.

VII. APPENDIX

A. Computational cost of UVTomo-GAN

Cost of projection generation: To generate $N_\theta = O(m)$ projection templates following (7), we first compute the inner summation over q , i.e.,

$$f_k(\xi_j) = \sum_{q=1}^{p_k} c_{k,q} J_{k,q}(\xi_j). \quad (32)$$

On the radial line, we have $O(m)$ equally spaced points ξ_j . Given that $K_{\max} = O(m)$ and $p_k = O(m)$, computing $f_k(\xi_j)$, $\forall k, j$ requires $O(m^3)$ computations.

Next, using $f_k(\xi_j)$ we compute the outer sum in (7) with respect to k for N_θ projection angles. A naive matrix multiplication implementation for this step leads to $O(m^3)$ cost (multiplying two matrices of size $O(m) \times O(m)$). This can be further reduced using FFT to $O(m^2 \log m)$. Finally, the total cost of generating N_θ projections using (7) is $O(m^3)$.

Note that for a naive implementation of the projection operator in spatial domain, the cost of generating N_θ projections would be $O(m^4)$. The projection operator along a specific direction θ can be represented by a $m \times m^2$ matrix. To attain one projection, we multiply this projection operator by the flattened image. This results in $O(m^3)$ cost. For N_θ projections, the total cost would then be $O(m^4)$.

B. Proof of Theorem 1

First we prove:

$$P_{f,p_f}^{\text{clean}} = P_{g,p_g}^{\text{clean}} \Rightarrow [f] = [g]. \quad (33)$$

From $P_{\text{clean}}[f, p_f] = P_{\text{clean}}[g, p_g]$, it is implied that the support of the two distributions are the same. This means that f and g have the same projection set. In other words, $\{\mathcal{P}_{\theta_i} f\}_{i=1}^{N_\theta} = \{\mathcal{P}_{\hat{\theta}_j} g\}_{j=1}^{N_\theta}$ where $\hat{\theta} = \{\hat{\theta}_j\}_{j=1}^{N_\theta}$ can be a shuffled version of $\theta = \{\theta_i\}_{i=1}^{N_\theta}$. Intuitively, one can imagine two objects f and g which have the same projection lines, however the order of the angles of f can be a shuffled version of the projection angles for g . Now the question that arises is: Given the class of functions f and g belong to, is it possible to have two distinct objects that produce identical projection sets?

This question is related to the feasibility of unique angle recovery in unknown view tomography, comprehensively studied in [6], [7]. Based on our discussions so far, we seek to prove the following:

$$\{\mathcal{P}_{\theta_i} f\}_{i=1}^{N_\theta} = \{\mathcal{P}_{\hat{\theta}_j} g\}_{j=1}^{N_\theta} \Rightarrow [f] = [g]. \quad (34)$$

In (34), the LHS implies that f and g have the same set of projection lines, in other words we have: $\forall \gamma \in \{\mathcal{P}_{\theta_i} f\}_{i=1}^{N_\theta}$, $\gamma \in \{\mathcal{P}_{\hat{\theta}_j} g\}_{j=1}^{N_\theta}$ and $\forall \gamma' \in \{\mathcal{P}_{\hat{\theta}_j} g\}_{j=1}^{N_\theta}$, $\gamma' \in \{\mathcal{P}_{\theta_i} f\}_{i=1}^{N_\theta}$. To prove the above, we borrow the definitions and various theoretical results in [6]. Helgasson–Ludwig (HL) consistency conditions [59] link the geometric moments of a 2D object to

its projections. Let v and μ define the geometric moment of the image f and its projection as:

$$v_{i,k}(f) = \int_{-1}^1 \int_{-1}^1 x^i y^k f(x, y) dx dy \quad (35)$$

$$\mu_d(\theta; f) = \int_{-1}^1 x^d \{\mathcal{P}_\theta f\}(x) dx. \quad (36)$$

Object moments of order d are the ones that satisfy $i+k=d$. Let $\mathbf{v}(f)$, denote the set of geometric moments of order $d \in D$ for object f . Given the object moments $\mathbf{v}(f)$, we construct a family of trigonometric polynomials as:

$$\mathcal{Q}_d(\theta; \mathbf{v}(f)) = \sum_{r=0}^d \binom{d}{r} v_{r,d-r}(f) (\cos \theta)^r (\sin \theta)^{d-r}. \quad (37)$$

Given the definition (37), we state the HL conditions as:

$$\mathcal{Q}_d(\theta; \mathbf{v}(f)) = \mu_d(\theta; f). \quad (38)$$

We have defined equivalence for 2D images before. If two images are equivalent, then they are related through a rotation and reflection. Similarly, we can define equivalence on the projection angles. Assume two vector of projection angles of length N_θ , $\theta, \hat{\theta} \in [-\pi, \pi]^{N_\theta}$. θ is said to be equivalent to $\hat{\theta}$, i.e., $\theta \sim \hat{\theta}$ if $\exists \eta \in \{-1, 1\}$ and $\alpha \in [-\pi, \pi]$ such that $\hat{\theta}_i = \eta \theta_i + \alpha + 2\pi n_i$, for $n_i \in \mathbb{Z}$.

As the projection set for f and g objects are the same (based on (34)), we conclude $\forall \theta, \exists \hat{\theta}$ such that:

$$\mu_d(\theta; f) = \mu_d(\hat{\theta}; g). \quad (39)$$

After invoking HL conditions (38) for object f on the RHS of (39) we get:

$$\mathcal{Q}_d(\theta; \mathbf{v}(f)) = \mu_d(\hat{\theta}; g), \quad \forall d \geq 0. \quad (40)$$

Note that, we have narrowed down the identical projection sets for f and g to (40). Now the question that arises is what is the relationship between θ and $\hat{\theta}$?

To find the answer to this question, we first limit the set of moment orders to $d \in D = \{1, 2\}$ (as (40) holds for $\forall d \geq 0$, we can simply do this). We now invoke Corollary 5 of Theorem 9 in [6]. We restate this corollary below.

Corollary 1 (Corollary 5 of Theorem 9 [6]): Suppose θ is a set of π -distinct view angles (there are no two angles that are different by a factor of π) and $N_\theta > 8$. Suppose \mathbf{v} satisfies the following condition: (i) $\nexists \beta, \gamma \in \mathbb{R}$ such that:

$$\mathcal{Q}_2(\theta; \mathbf{v}) = \beta (\mathcal{Q}_1(\theta; \mathbf{v}))^2 + \gamma, \quad \forall \theta \in [0, \pi] \quad (41)$$

or equivalently,

$$\det \begin{bmatrix} v_{1,0}^2 & v_{2,0} & 1 \\ 2v_{1,0}v_{0,1} & v_{1,1} & 0 \\ v_{0,1}^2 & v_{0,2} & 1 \end{bmatrix} \neq 0. \quad (42)$$

If $\theta \notin \text{UAS}(\mathbf{v})$ with UAS (unidentifiable angle set) defined as:

$$\text{UAS}(\mathbf{v}) = \left\{ \arg \left(\sqrt{\frac{-c_1^*}{c_1}} \right), \arg \left(-\sqrt{\frac{-c_1^*}{c_1}} \right) \right\} \quad (43)$$

where,

$$c_1 = \frac{1}{2}(v_{1,0} - i v_{0,1}) \quad (44)$$

then, the only view angles $\hat{\theta}$ that produce the same projection moments of order $D = \{1, 2\}$ are equivalent to θ . This implies

that $\theta \sim \hat{\theta}$. \square

Adhering to Corollary 1, if $\mathbf{v}(f)$ satisfies the conditions in (41) or (42), then for $d \in \{1, 2\}$, the only projection angles $\hat{\theta}$ for which (40) holds are equivalent to θ and thus $\theta \sim \hat{\theta}$. On the other hand, based on Corollary 1, the projection angles recovered for f , i.e., θ are equivalent to the GT projection angles $\check{\theta}$ used for generating the projection lines of f , i.e., $\theta \sim \check{\theta}$. Based on the transitivity property of equivalence relation, this leads to $\hat{\theta} \sim \check{\theta}$

Given $\theta \sim \hat{\theta} \sim \check{\theta}$ and the fact that the projection sets corresponding to the objects f and g are identical, the objects \hat{f} and \hat{g} reconstructed from the projection sets and projection angles would also be the same (up to a rotation and reflection), i.e., $[\hat{f}] = [\hat{g}]$. We now link the reconstructed objects and their ground truths.

If we have sufficiently large N_θ , we can directly recover HB expansion coefficients c by solving a set of linear equations linking the projection lines to the HB expansion coefficients. Given the HB expansion coefficients, we have a continuous representation of the image as defined in (10). This leads to $\hat{f} = f$ and $\hat{g} = g$ and finally concludes $[f] = [g]$.

As $[f] = [g]$, $\exists \Gamma \in O(2)$ such that $g = \Gamma f$. $P_{f,p_f}^{\text{clean}} = P_{g,p_g}^{\text{clean}}$ implies the TV distance between the two probability distributions is zero, i.e.,

$$TV(P_{f,p_f}^{\text{clean}}, P_{\Gamma f,p_g}^{\text{clean}}) = 0. \quad (45)$$

Invoking Lemma 1 (stated in Appendix VII-D), we know $P_{\text{clean}}[\Gamma f, p_g] = P_{\text{clean}}[f, \Gamma^{-1}p_g]$, therefore (45) becomes,

$$TV(P_{f,p_f}^{\text{clean}}, P_{f,\Gamma^{-1}p_g}^{\text{clean}}) = TV(p_f, \Gamma^{-1}p_g) = \frac{1}{2} \|p_f - \Gamma^{-1}p_g\|_1. \quad (46)$$

Following (45), the LHS of (46) is 0. Thus, based on the non-negativity property of $\|\cdot\|_1$ norm, we have,

$$p_f = \Gamma^{-1}p_g \Rightarrow p_g = \Gamma p_f \quad (47)$$

implying $[p_f] = [p_g]$. \blacksquare

C. Proof of Theorem 2

Our proof follows closely the proof of Theorem 1 in [36]. We first show that,

$$P_{f,p}^{\text{noisy}} = P_{\tilde{f},\tilde{p}}^{\text{noisy}} \Rightarrow P_{f,p}^{\text{clean}} = P_{\tilde{f},\tilde{p}}^{\text{clean}}. \quad (48)$$

According to the forward model (1), we have $\zeta = \mathcal{P}_\theta f + \varepsilon$ where $\varepsilon[n] \sim q_\varepsilon$ an additive white Gaussian noise which is independent of f and $\theta \sim p$. Note that we are considering a general model for the noise and not confining it to be a Gaussian. As ε is independent of the image and projection angles, we have:

$$P_{f,p}^{\text{noisy}} = P_{f,p}^{\text{clean}} * q_\varepsilon \quad (49)$$

In Fourier domain, (49) becomes:

$$\mathcal{F}\{P_{f,p}^{\text{noisy}}\} = \mathcal{F}\{P_{f,p}^{\text{clean}}\} \mathcal{F}\{q_\varepsilon\}. \quad (50)$$

We have assumed ε to have full support in Fourier domain, therefore we can divide both sides of (50) by $\mathcal{F}\{q_\varepsilon\}$. Therefore given $\mathcal{F}\{P_{f,p}^{\text{noisy}}\}$, we have $\mathcal{F}\{P_{f,p}^{\text{clean}}\}$ and (48) is proved. Now, we show:

$$P_{f,p}^{\text{clean}} = P_{\tilde{f},\tilde{p}}^{\text{clean}} \Rightarrow \tilde{f} = \Gamma f \text{ and } \tilde{p} = \Gamma p \quad (51)$$

for a unique $\Gamma \in O(2)$. To prove (51), we invoke Theorem 1. Theorem 1 states that if the two images f and \tilde{f} have the

same distribution of the clean projections, then the objects and their associated projection distributions are equivalent up to a rotation and reflection. This confirms $[f] = [\tilde{f}]$, and $[p] = [\tilde{p}]$, i.e., $\tilde{f} = \Gamma f$ and $\tilde{p} = \Gamma p$, for a $\Gamma \in O(2)$. \blacksquare

D. Lemma 1

Assume $f \in \mathcal{L}_1(\mathbb{B}_2) \cap \mathcal{L}_2(\mathbb{B}_2)$, projection angles θ are distributed following p , i.e. $\theta \sim p$ and $\Gamma \in O(2)$. Then,

$$P_{f,\Gamma^{-1}p}^{\text{clean}} = P_{\Gamma f,p}^{\text{clean}} \quad (52)$$

Proof: For a given (f, p_f) , if $\gamma \in O(2)$ is applied to both f and p , then the induced probability distribution of the projection images would be the same, i.e. $P_{f,p}^{\text{clean}} = P_{\Gamma f,\Gamma p}^{\text{clean}}$. After changing $p' = \Gamma p$, we have $P_{f,\Gamma^{-1}p'}^{\text{clean}} = P_{\Gamma f,p'}^{\text{clean}}$, thus concluding the proof.

REFERENCES

- [1] H. Stark, J. Woods, I. Paul, and R. Hingorani, "Direct Fourier reconstruction in computer tomography," *IEEE Transactions on Acoustics, Speech, and Signal Processing*, vol. 29, no. 2, pp. 237–245, 1981.
- [2] E. Y. Sidky and X. Pan, "Image reconstruction in circular cone-beam computed tomography by constrained, total-variation minimization," *Physics in Medicine and Biology*, vol. 53, pp. 4777–4807, aug 2008.
- [3] S. Niu, Y. Gao, Z. Bian, J. Huang, W. Chen, G. Yu, Z. Liang, and J. Ma, "Sparse-view x-ray CT reconstruction via total generalized variation regularization," *Physics in Medicine and Biology*, vol. 59, pp. 2997–3017, May 2014.
- [4] H. Zhang, J. Wang, D. Zeng, X. Tao, and J. Ma, "Regularization strategies in statistical image reconstruction of low-dose x-ray ct: A review," *Medical Physics*, vol. 45, no. 10, pp. e886–e907, 2018.
- [5] C. Gong and L. Zeng, "Adaptive iterative reconstruction based on relative total variation for low-intensity computed tomography," *Signal Processing*, vol. 165, pp. 149 – 162, 2019.
- [6] S. Basu and Y. Bresler, "Uniqueness of tomography with unknown view angles," *IEEE Transactions on Image Processing*, vol. 9, no. 6, pp. 1094–1106, 2000.
- [7] S. Basu and Y. Bresler, "Feasibility of tomography with unknown view angles," *IEEE Transactions on Image Processing*, vol. 9, no. 6, pp. 1107–1122, 2000.
- [8] Y. Fang, S. Murugappan, and K. Ramani, "Estimating view parameters from random projections for tomography using spherical mds," *BMC Medical Imaging*, vol. 10, no. 1, p. 12, 2010.
- [9] R. R. Coifman, Y. Shkolnisky, F. J. Sigworth, and A. Singer, "Graph laplacian tomography from unknown random projections," *IEEE Transactions on Image Processing*, vol. 17, no. 10, pp. 1891–1899, 2008.
- [10] B. B. Cheikh, E. Baudrier, and G. Frey, "A tomographical reconstruction method from unknown direction projections for 2D gray-level images," *Pattern Recognition Letters*, vol. 86, pp. 49 – 55, 2017.
- [11] M. Zehni, S. Huang, I. Dokmanić, and Z. Zhao, "Geometric invariants for sparse unknown view tomography," in *ICASSP 2019 - 2019 IEEE International Conference on Acoustics, Speech and Signal Processing (ICASSP)*, pp. 5027–5031, 2019.
- [12] M. Zehni, S. Huang, I. Dokmanić, and Z. Zhao, "3D unknown view tomography via rotation invariants," in *ICASSP 2020 - 2020 IEEE International Conference on Acoustics, Speech and Signal Processing (ICASSP)*, pp. 1449–1453, 2020.
- [13] E. Levin, T. Bendory, N. Boumal, J. Kileel, and A. Singer, "3D ab initio modeling in cryo-EM by autocorrelation analysis," in *2018 IEEE 15th International Symposium on Biomedical Imaging (ISBI 2018)*, pp. 1569–1573, 2018.
- [14] L. Wang and Z. Zhao, "Two-dimensional tomography from noisy projection tilt series taken at unknown view angles with non-uniform distribution," in *2019 IEEE International Conference on Image Processing (ICIP)*, pp. 1242–1246, 2019.
- [15] G. Wang, J. C. Ye, and B. De Man, "Deep learning for tomographic image reconstruction," *Nature Machine Intelligence*, vol. 2, no. 12, pp. 737–748, 2020.
- [16] B. Zhu, J. Z. Liu, S. F. Cauley, B. R. Rosen, and M. S. Rosen, "Image reconstruction by domain-transform manifold learning," *Nature*, vol. 555, no. 7697, pp. 487–492, 2018.

- [17] Y. Ge, T. Su, J. Zhu, X. Deng, Q. Zhang, J. Chen, Z. Hu, H. Zheng, and D. Liang, "Adaptive-net: deep computed tomography reconstruction network with analytical domain transformation knowledge," *Quantitative Imaging in Medicine and Surgery*, vol. 10, no. 2, 2020.
- [18] T. Würfl, F. C. Ghesu, V. Christlein, and A. Maier, "Deep learning computed tomography," in *Medical Image Computing and Computer-Assisted Intervention - MICCAI 2016* (S. Ourselin, L. Joskowicz, M. R. Sabuncu, G. Unal, and W. Wells, eds.), (Cham), pp. 432–440, Springer International Publishing, 2016.
- [19] K. H. Jin, M. T. McCann, E. Froustey, and M. Unser, "Deep convolutional neural network for inverse problems in imaging," *IEEE Transactions on Image Processing*, vol. 26, no. 9, pp. 4509–4522, 2017.
- [20] T. M. Quan, T. Nguyen-Duc, and W. Jeong, "Compressed sensing MRI reconstruction using a generative adversarial network with a cyclic loss," *IEEE Transactions on Medical Imaging*, vol. 37, no. 6, pp. 1488–1497, 2018.
- [21] H. Chen, Y. Zhang, M. K. Kalra, F. Lin, Y. Chen, P. Liao, J. Zhou, and G. Wang, "Low-dose CT with a residual encoder-decoder convolutional neural network," *IEEE Transactions on Medical Imaging*, vol. 36, no. 12, pp. 2524–2535, 2017.
- [22] H. Shan, A. Padole, F. Homayounieh, U. Kruger, R. D. Khera, C. Nitiwarangkul, M. K. Kalra, and G. Wang, "Competitive performance of a modularized deep neural network compared to commercial algorithms for low-dose CT image reconstruction," *Nature Machine Intelligence*, vol. 1, no. 6, pp. 269–276, 2019.
- [23] Y. Han and J. C. Ye, "Framing U-net via deep convolutional framelets: Application to sparse-view CT," *IEEE Transactions on Medical Imaging*, vol. 37, no. 6, pp. 1418–1429, 2018.
- [24] E. Kang, W. Chang, J. Yoo, and J. C. Ye, "Deep convolutional framelet denosing for low-dose CT via wavelet residual network," *IEEE Transactions on Medical Imaging*, vol. 37, no. 6, pp. 1358–1369, 2018.
- [25] Q. Yang, P. Yan, Y. Zhang, H. Yu, Y. Shi, X. Mou, M. K. Kalra, Y. Zhang, L. Sun, and G. Wang, "Low-dose CT image denoising using a generative adversarial network with wasserstein distance and perceptual loss," *IEEE Transactions on Medical Imaging*, vol. 37, no. 6, pp. 1348–1357, 2018.
- [26] A. Zhong, B. Li, N. Luo, Y. Xu, L. Zhou, and X. Zhen, "Image restoration for low-dose CT via transfer learning and residual network," *IEEE Access*, vol. 8, pp. 112078–112091, 2020.
- [27] J. Dong, J. Fu, and Z. He, "A deep learning reconstruction framework for x-ray computed tomography with incomplete data," *PLOS ONE*, vol. 14, p. e0224426, 11 2019.
- [28] Z. Li, A. Cai, L. Wang, W. Zhang, C. Tang, L. Li, N. Liang, and B. Yan, "Promising generative adversarial network based sinogram inpainting method for ultra-limited-angle computed tomography imaging," *Sensors*, vol. 19, no. 18, p. 3941, 2019.
- [29] J. Adler and O. Ozan, "Solving ill-posed inverse problems using iterative deep neural networks," *Inverse Problems*, vol. 33, 04 2017.
- [30] J. Adler and O. Öktem, "Learned primal-dual reconstruction," *IEEE Transactions on Medical Imaging*, vol. 37, no. 6, pp. 1322–1332, 2018.
- [31] X. Yang, M. Kahnt, D. Brückner, A. Schropp, Y. Fam, J. Becher, J.-D. Grunwaldt, T. L. Sheppard, and C. G. Schroer, "Tomographic reconstruction with a generative adversarial network," *Journal of Synchrotron Radiation*, vol. 27, pp. 486–493, Mar 2020.
- [32] D. Ulyanov, A. Vedaldi, and V. Lempitsky, "Deep image prior," in *Proceedings of the IEEE Conference on Computer Vision and Pattern Recognition (CVPR)*, June 2018.
- [33] D. Otero Bague, J. Leuschner, and M. Schmidt, "Computed tomography reconstruction using deep image prior and learned reconstruction methods," *Inverse Problems*, vol. 36, 03 2020.
- [34] K. Gong, C. Catana, J. Qi, and Q. Li, "Pet image reconstruction using deep image prior," *IEEE Transactions on Medical Imaging*, vol. 38, no. 7, pp. 1655–1665, 2019.
- [35] I. Goodfellow, J. Pouget-Abadie, M. Mirza, B. Xu, D. Warde-Farley, S. Ozair, A. Courville, and Y. Bengio, "Generative adversarial nets," in *Advances in Neural Information Processing Systems 27* (Z. Ghahramani, M. Welling, C. Cortes, N. D. Lawrence, and K. Q. Weinberger, eds.), pp. 2672–2680, Curran Associates, Inc., 2014.
- [36] H. Gupta, M. T. McCann, L. Donati, and M. Unser, "CryoGAN: A new reconstruction paradigm for single-particle cryo-EM via deep adversarial learning," *bioRxiv*, 2020.
- [37] E. Jang, S. Gu, and B. Poole, "Categorical Reparameterization with Gumbel-Softmax," *ICLR*, 2017.
- [38] M. Zehni and Z. Zhao, "MSR-GAN: Multi-segment reconstruction via adversarial learning," in *ICASSP 2021 - 2021 IEEE International Conference on Acoustics, Speech and Signal Processing (ICASSP)*, pp. 5115–5119, 2021.
- [39] E. D. Zhong, T. Bepler, B. Berger, and J. H. Davis, "CryoDRGN: reconstruction of heterogeneous cryo-EM structures using neural networks," *Nature Methods*, vol. 18, no. 2, pp. 176–185, 2021.
- [40] L. Greengard and J.-Y. Lee, "Accelerating the nonuniform fast fourier transform," *SIAM review*, vol. 46, no. 3, pp. 443–454, 2004.
- [41] Z. Zhao, Y. Shkolnisky, and A. Singer, "Fast steerable principal component analysis," *IEEE Transactions on Computational Imaging*, vol. 2, no. 1, pp. 1–12, 2016.
- [42] A. Klug and R. Crowther, "Three-dimensional image reconstruction from the viewpoint of information theory," *Nature*, vol. 238, no. 5365, pp. 435–440, 1972.
- [43] M. Arjovsky, S. Chintala, and L. Bottou, "Wasserstein generative adversarial networks," in *Proceedings of the 34th International Conference on Machine Learning-Volume 70*, pp. 214–223, 2017.
- [44] I. Gulrajani, F. Ahmed, M. Arjovsky, V. Dumoulin, and A. Courville, "Improved training of wasserstein GANs," in *Proceedings of the 31st International Conference on Neural Information Processing Systems, NIPS'17*, (Red Hook, NY, USA), p. 5769–5779, Curran Associates Inc., 2017.
- [45] T. Miyato, T. Kataoka, M. Koyama, and Y. Yoshida, "Spectral normalization for generative adversarial networks," in *International Conference on Learning Representations*, 2018.
- [46] A. Punjani, M. A. Brubaker, and D. J. Fleet, "Building proteins in a day: Efficient 3D molecular structure estimation with electron cryomicroscopy," *IEEE Transactions on Pattern Analysis and Machine Intelligence*, vol. 39, no. 4, pp. 706–718, 2017.
- [47] A. Barnett, L. Greengard, A. Pataki, and M. Spivak, "Rapid solution of the cryo-EM reconstruction problem by frequency marching," *SIAM Journal on Imaging Sciences*, vol. 10, 10 2016.
- [48] L. Wang, Y. Shkolnisky, and A. Singer, "A Fourier-based approach for iterative 3D reconstruction from cryo-EM images," *arXiv preprint arXiv:1307.5824*, 2013.
- [49] L. Donati, M. Nilchian, C. O. S. Sorzano, and M. Unser, "Fast multiscale reconstruction for cryo-EM," *Journal of Structural Biology*, vol. 204, no. 3, pp. 543–554, 2018.
- [50] S. H. Scheres, "Relion: Implementation of a Bayesian approach to cryo-EM structure determination," *Journal of Structural Biology*, vol. 180, no. 3, pp. 519–530, 2012.
- [51] T. R. Moen, B. Chen, D. R. Holmes III, X. Duan, Z. Yu, L. Yu, S. Leng, J. G. Fletcher, and C. H. McCollough, "Low-dose CT image and projection dataset," *Medical Physics*, vol. 48, no. 2, pp. 902–911, 2021.
- [52] B. Beckert, M. Turk, A. Czech, O. Berninghausen, R. Beckmann, Z. Ignatova, J. M. Plitzko, and D. N. Wilson, "Structure of a hibernating 100s ribosome reveals an inactive conformation of the ribosomal protein s1," *Nature Microbiology*, vol. 3, no. 10, pp. 1115–1121, 2018.
- [53] E. F. Pettersen, T. D. Goddard, C. C. Huang, G. S. Couch, D. M. Greenblatt, E. C. Meng, and T. E. Ferrin, "UCSF Chimera—a visualization system for exploratory research and analysis," *Journal of computational chemistry*, vol. 25, p. 1605–1612, October 2004.
- [54] A. Averbuch, R. Coifman, D. Donoho, M. Elad, and M. Israeli, "Fast and accurate polar fourier transform," *Applied and Computational Harmonic Analysis*, vol. 21, no. 2, pp. 145–167, 2006.
- [55] B. Xu, N. Wang, T. Chen, and M. Li, "Empirical evaluation of rectified activations in convolutional network," *arXiv preprint arXiv:1505.00853*, 2015.
- [56] S. Boyd, N. Parikh, and E. Chu, *Distributed optimization and statistical learning via the alternating direction method of multipliers*. Now Publishers Inc, 2011.
- [57] E. Soubies, F. Soulez, M. T. McCann, T. Pham, L. Donati, T. Debarre, D. Sage, and M. Unser, "Pocket guide to solve inverse problems with GlobalBiolm," *Inverse Problems*, vol. 35, p. 104006, sep 2019.
- [58] A. Bora, E. Price, and A. G. Dimakis, "AmbientGAN: Generative models from lossy measurements," in *International Conference on Learning Representations*, 2018.
- [59] F. Natterer, *The Mathematics of Computerized Tomography*. Society for Industrial and Applied Mathematics, 2001.